Theoretical and Applied Fracture Mechanics 147 (2026) 105843

Contents lists available at ScienceDirect

Theoretical and Applied Fracture Mechanics

journal homepage: www.elsevier.com/locate/tafmec

Through-thickness 3D-printed bio-inspired fibers to enhance mode I fracture resistance of composite bonded joints

Zhiyuan Xu [a], Ran Tao [a], Kunal Masania [b], Sofia Teixeira de Freitas [a,c,*]

[a] Faculty of Aerospace Engineering, Delft University of Technology, Delft 2629 HS, Netherlands
[b] Shaping Matter Lab, Faculty of Aerospace Engineering, Delft University of Technology, Delft 2629 HS, Netherlands
[c] IDMEC, Instituto Superior Técnico, Universidade de Lisboa, Lisboa, Portugal

ARTICLE INFO

Dataset link: 10.4121/35b19ead-8133-4255-99e9-adc14222b738

Keywords:
Toughness
Biomimetic fibers
Bonded joints
Composites

ABSTRACT

Composite bonded joints are susceptible to sudden and brittle failure, especially under mode I opening loading conditions. To improve crack resistance under mode I, conventional solutions use through-thickness reinforcements, such as rivets, which is effective in delaying the crack growth but damage the performance of the composite. This study explores an alternative through-thickness reinforcement consisting of 3D-printed overlapping curl (OC) fibers with sacrificial bonds and hidden lengths (SBHL) to enhance fracture resistance under mode I of composite bonded joints. The OC fibers are embedded through the thickness of a structural epoxy, oriented perpendicular to the crack propagation direction, enabling effective activation of hidden length unfolding under mode I opening conditions. This through-thickness reinforcement fully exploits the SBHL toughening mechanism without introducing detrimental effects to the CFRP substrate, in contrast to conventional techniques such as Z-pinning or riveting. Double cantilever beam experiments demonstrate that the OC topology is essential for effective toughening, as it anchors the OCs within the adhesive and prevents pull-out, allowing hidden length unfolding that leads to extended crack bridging distance and increases the mode I energy release rate by up to 119 %. Furthermore, numerical simulations are conducted to systematically explore the influence of OC mechanical parameters, providing design guidelines for improving the fracture performance of CFRP adhesively bonded joints.

1. Introduction

Carbon fiber reinforcement polymer (CFRP) composites have been widely used in structural components, such as in aircraft, automotive, and marine structures [1] due to their high specific strength and stiffness [2,3]. Large engineering components made from CFRP are typically assembled using mechanical fasteners, co-bonding, or secondary bonding techniques. In the case of primary structures, secondary bonding is used along with bolts or rivets, used as crack stoppers, to avoid sudden failure of the bondline [4,5]. However, mechanical fasteners require drilling holes in the CFRP, which may cause delamination and stress concentrations around the fastener sites. In addition, the use of fasteners adds extra weight to the composite structure, potentially resulting in damage initiation and reduced load capacity [6]. In contrast, adhesive bonding is a promising joining technique that offers uniform stress distribution, lightweight, and enhanced structural integrity [7]. Nevertheless, the reliable detection of weak adhesion remains limited for most non-destructive testing (NDT) techniques (e.g., ultrasonic C-scans), particularly for defects such as kissing bonds, and strongly depends on both the defect types and the inspection method employed [8]. These challenges demand incorporating crack-arresting features to slow or prevent crack growth, thereby improving damage tolerance in composite adhesive joints for broader industrial applications.

Methods for improving the design and crack resistance of adhesive-bonded joints have been extensively studied. Z-pinning or stitching is a widely studied strategy to prevent delamination and crack growth in composites [9–11]. By inserting reinforced conductive pins through the thickness of adhesive-bonded composite lap joints, crack growth can be inhibited via extrinsic energy dissipation, while also providing self-sensing capabilities [9]. However, through-thickness pins may cause stress concentrations in the substrate and increase fiber breakage due to fiber waviness [10]. Moreover, Z-pins are limited to co-cured joints and have restricted applicability in secondary bonded joints, where components are already cured. Architecting the adhesive bondline offers an alternative approach to introducing crack-arresting features. For example, Maloney et al. [12] introduced periodic stop holes in the

* Corresponding author.
E-mail addresses: s.teixeiradefreitas@tudelft.nl, sofia.teixeira.freitas@tecnico.ulisboa.pt (S. Teixeira de Freitas).

https://doi.org/10.1016/j.tafmec.2026.105843
Received 22 May 2026; Received in revised form 9 July 2026; Accepted 27 July 2026
Available online 19 August 2026

adhesive layer, arresting crack growth and increasing fracture toughness by up to 50 %. They also incorporated a woven copper wire mesh into the adhesive layer, which acted as a bridging element to impede crack growth and enhance the energy release rate [12]. Similar approaches include embedding thermoplastic inclusions [13], polyamide straight wires [14], 2D woven nets [3,13], and natural fibers [15] into the bondline, all of which successfully hinder crack propagation and significantly improve joint fracture performance. Nevertheless, these inclusions typically feature simple geometries and lack tailored design features intended to activate specific toughening mechanisms.

Natural materials, known for their exceptional strength and toughness, have inspired researchers to develop new design architectures for improving the mechanical properties of engineering materials and interfaces [16–20]. One example of nature's excellent energy absorption ability is found in spider silk. Its molecular structure, containing sacrificial bonds and hidden lengths (SBHL), enables a sequential process where sacrificial bonds (e.g., hydrogen bonds) break first, followed by the gradual unfolding of hidden lengths under stress, allowing for high extensibility and energy absorption [21] before final failure. The application of the SBHL toughening mechanisms has been used to toughen elastomers [22,23]. By integrating 3D-printed biomimetic SBHL structures into polydimethylsiloxane (PDMS), increases of more than 17-fold in extensibility and 15-fold in fracture resistance have been reported. These remarkable improvements originate from the progressive activation of sacrificial bonds and hidden lengths, which dissipate energy and delay crack propagation. However, existing studies have been limited to highly deformable soft materials undergoing large strains. The potential of SBHL-inspired architectures as through-thickness reinforcements for structural adhesively bonded composite joints, where crack bridging rather than bulk deformation governs fracture resistance, has not yet been explored.

The authors have been the first to apply this concept to structural epoxies. Firstly, as reinforcement fibers of an unconfined biobased epoxy [24], where it is demonstrated that SBHL structures can be triggered and the hidden length unfolds in rigid structural bulk epoxy, which experiences only small strains. Secondly, these fibers have been applied as a horizontal reinforcement into biobased epoxy adhesives. There was an improvement in mode I the fracture resistance; however, the crack growth remain unstable due to the brittle nature of the biobased epoxy and the limited design of the horizontal reinforcement [25].

In this study, to further enhance the effectiveness of the OC fibers to retard crack growth under mode I in adhesively bonded joints, these OC reinforcements are, for the first time, integrated through the thickness of a structural epoxy adhesive bondline in composite bonded joints. Double cantilever beam (DCB) tests are employed to evaluate the mode I fracture resistance of the joints within a linear elastic fracture mechanics framework, where the energy release rate (ERR) is used as the primary measure of crack growth resistance. Under opening-mode loading, the through-thickness OCs, oriented perpendicular to the crack propagation direction, effectively activate hidden length unfolding and tensile crack bridging behavior. The effects of 3D-printing material selection and OC topology on joint fracture resistance and the associated toughening mechanisms are systematically investigated. Moreover, cohesive zone-based numerical models are developed to assess the roles of OC failure load and hidden length in governing the bridging response and ERR enhancement. Based on these results, design guidelines are proposed for optimizing OC-reinforced adhesively bonded joints.

2. Materials and specimens

2.1. Materials

The DCB substrate was manufactured from unidirectional carbon fiber prepregs Hexply 8552 – AS4 toughened epoxy resin (Hexcel Composites, Cambridge, UK). In order to manufacture the CFRP substrates, eight plies of the CFRP prepreg were stacked by hand layup in the 0-degree direction. The CFRP laminates were then cured in an autoclave on a flat aluminum plate under 5 bars of pressure and 180 °C for 120 mins. After curing, the CFRP plates were cut into the DCB substrate with dimensions: $205 \times 25 \times 1.5\ \mathrm{mm}^3$ (length×width×height). Then, on the smooth side of the substrate, the surface was carefully sanded with 360-grit sandpaper in a criss-cross pattern and cleaned with a soaked acetone tissue. The spider silk-inspired overlapping curl (OC) structures were manufactured using commercial polylactic acid (PLA, ReForm™ - rPLA) filament sourced from Formfutura BV (Nijmegen, Netherlands), while the polyamide filament, primarily composed of Polyamide 6 (PA6, F3 PA Pure Pro), was obtained from Fiberthree GmbH (Darmstadt, Germany). PLA and PA6 were selected to investigate the influence of printing-material ductility on the toughening performance of the OC reinforcements. PLA is one of the most widely used materials in fused filament fabrication and exhibits relatively low ductility (fracture strain ≈ 0.033) [26], providing a practical baseline material for comparison. In contrast, PA6 possesses significantly higher ductility (fracture strain > 2) [26], which is expected to facilitate hidden length unfolding and sustain crack bridging loads over larger displacements. The use of these two materials, therefore, enables a systematic comparison between brittle and ductile OC reinforcements and allows the role of material deformation capacity in activating the SBHL toughening mechanism to be assessed. The bi-component epoxy adhesive Araldite 2015/1, supplied by Huntsman International LLC, was used to secondary bond the CFRP substrates.

2.2. 3D-printed overlapping curl

Adopting the coiling rope effect [27], together with 3D-printing fused filament fabrication in 3D printer Prusa i3 MK3S+ with a nozzle size 0.4 mm, OC structures were manufactured containing coiling fibers with sacrificial bonds and hidden lengths with PLA and PA6, as shown in Fig. 1(a). The printing parameters, including the nozzle height (Z), nozzle moving speed (F), and filament extrusion value (E), were carefully optimized through iterative trial-and-error experiments to achieve the desired OC geometry while maintaining dimensional accuracy within the limited adhesive bondline thickness. These parameters were selected primarily to ensure the successful fabrication and integration of the OC structures into the bonded joints. It should be noted that the printing parameters may also influence the mechanical response of the OC structures by affecting filament dimensions, the formation of sacrificial bonds, and the hidden lengths. A detailed investigation of the relationships between printing parameters and the mechanical behavior of OC structures, including their effects on failure load and hidden length activation, has been reported in our previous work [26]. Therefore, the present study focuses on the application of the optimized OC structures in composite adhesively bonded joints rather than on further optimization of the printing process.

During fabrication, the nozzle temperature was intentionally set below the standard printing temperatures of PLA (210 °C) and PA6 (275 °C) to regulate the strength of the sacrificial bonds. These bonds are formed through localized fusion between adjacent filaments: after the lower filament is deposited, the subsequently extruded filament gradually contacts it under gravity, creating inter-filament junctions that act as sacrificial bonds. The strength of these junctions depends on the degree of polymer fusion and chain interdiffusion at the contact interface. Higher printing temperatures maintain the extruded filament in a molten state for a longer time, promoting inter-filament fusion and producing stronger sacrificial bonds. Conversely, lower printing temperatures accelerate filament cooling, thereby limiting interfacial fusion and reducing junction strength. As a result, relatively weak sacrificial bonds can be introduced into the OC structure, facilitating bond break and subsequent hidden length unfolding during DCB loading. To understand the effect of the OC topology on the fracture resistance improvement, straight fibers with a similar filament diameter were also

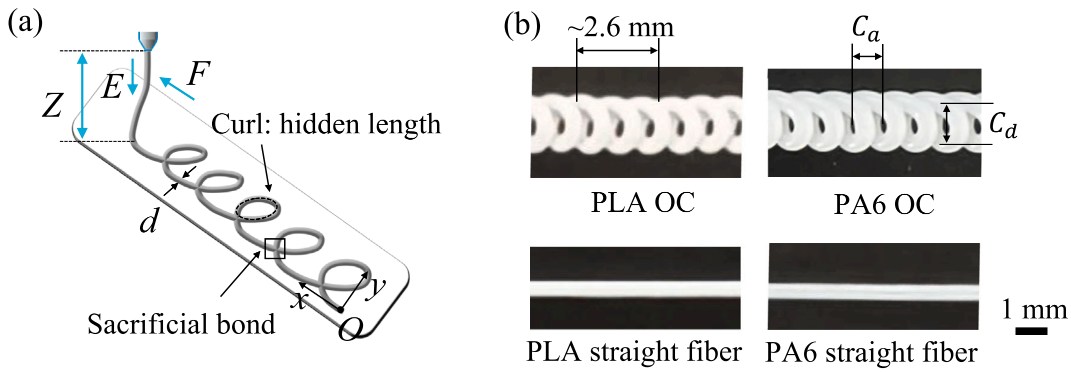

Fig. 1. (a) The 3D-printing process schematic of overlapping curl fabrication. (b) The geometry of printed overlapping curl and straight fiber structures.

Table 1
The 3D-printing parameters and geometric details of the straight fiber and overlapping curls. Z: nozzle height, F: nozzle moving speed, and E: filament extrusion value. d: the OC filament diameter, C_a: the pitch distance between curls, and C_d: the diameter of the curl.

Nomenclature	PLA-Straight	PLA-OC	PA6-Straight	PA6-OC
Nozzle temperature, (°C)	180	180	225	225
Nozzle height, Z (mm)	3	3	3	3
Nozzle moving speed, F (mm/min)	1500	60	1500	160
Filament extrusion value, E (mm/min)	20	110	20	110
Printed filament diameter, d (mm)	0.56 ± 0.02	0.55 ± 0.02	0.54 ± 0.01	0.57 ± 0.02
Curl pitch, C_a (mm)	–	0.97 ± 0.03	–	1.01 ± 0.02
Curl diameter, C_d (mm)	–	1.22 ± 0.01	–	1.22 ± 0.02
Curl: hidden length (mm)	–	3.14 ± 0.02	–	3.13 ± 0.03

printed for comparison. A close observation of the printed overlapping curl and straight fiber structures are shown in Fig. 1(b) and the specific parameters of these structures are listed in Table 1. C_a is the pitch distance between curls and C_d is the diameter of the curl.

2.3. DCB specimens fabrication

The previously printed overlapping curls were cut into smaller segments containing three adjacent curls with a total length around 2.6 mm. For comparison, straight fibers were also cut into smaller segments of the same length. Then, to accommodate the geometry of the OC segments, the DCB bondline thickness was selected as 2.6 mm accordingly.

The fabrication process of one DCB sample is shown in Fig. 2 as an example. A thin layer of cyanoacrylate instantaeous adhesive (CC-33 A, KYOWA Electronic Instruments Co., LTD, Japan) was used to bond the bottom end of the OC to the bottom CFRP substrate. Following this method, OCs were evenly placed vertically (in the z-direction) along the substrate: 2 along the width in the y-direction and every 5 mm along the length in the x-direction. In total, 20 overlapping curls were integrated in each DCB sample in the area of 25 mm width by 45 mm length reinforced region. After positioning the OCs within the reinforcement region, the substrate surfaces were exposed to an in-house UV/ozone treatment for 7 min, following the procedure described in [28,29]. The purpose of the UV/ozone treatment is to remove organic contaminants from the laminate surface and introduce polar oxygen-containing functional groups, thereby increasing the surface energy and improving wettability. These surface modifications enhance the interfacial adhesion between the CFRP substrates and the adhesive, promoting cohesive failure within the adhesive layer rather than adhesive failure at the substrate–adhesive interface during crack propagation. Spacers with thickness 2.6 mm were fixed onto the two extremities of the substrate to control the bondline thickness. In addition, a 10 mm razor blade was placed into the center of the bondline to create a pre-crack. After extruding the Araldite 2015-1 adhesive onto the bottom substrate containing the OCs, we placed the upper substrate on top and added weights to apply mechanical pressure, ensuring intimate contact. As a result, the OCs were embedded through the thickness of the adhesive bondline. Finally, the assembled DCB samples were put into the oven at 80 °C for 1 h for the adhesive to be cured. In total, four DCB sample configurations were manufactured with different reinforcement materials and topologies, designated as DCB-PLA-Straight and DCB-PA6-Straight for straight fibers, and DCB-PLA-OC and DCB-PA6-OC for overlapping curls. For comparison, reference DCB specimens without reinforcement were also manufactured and were hereafter named as DCB-Pure. Post-mortem scanning electron microscopy (SEM, JSM-7500F, JEOL Co., Japan) was employed to visualize the fracture surface morphological characteristics of reinforced straight fibers and overlapping curls after testing.

3. Experimental methods

3.1. Overlapping curl tensile test

In order to determine the tensile behavior of the OC alone, tensile tests were performed. A Zwick electro-mechanical testing machine with a 100 N load cell was used to characterize the mechanical properties of the straight fiber and overlapping curl under uniaxial tensile conditions. The reader can refer to [26] for the sample preparation. A minimum of 5 samples were tested with a testing speed of 2 mm/min. The experiment setup is shown in Fig. 3(a).

3.2. DCB test

A Zwick electro-mechanical testing machine with a 1 kN load cell was used to perform the DCB quasi-static tests under mode I loading. A testing speed of 2 mm/min was applied, as recommended by the standard ASTM D5528 [30]. At least 5 samples of each DCB configuration were tested. Fig. 3(b) shows the DCB experiment setup. The crack propagation was recorded by a camera in the front view of the DCB sample and a traveling microscope was placed to capture a side view of the fracture process every 4 s.

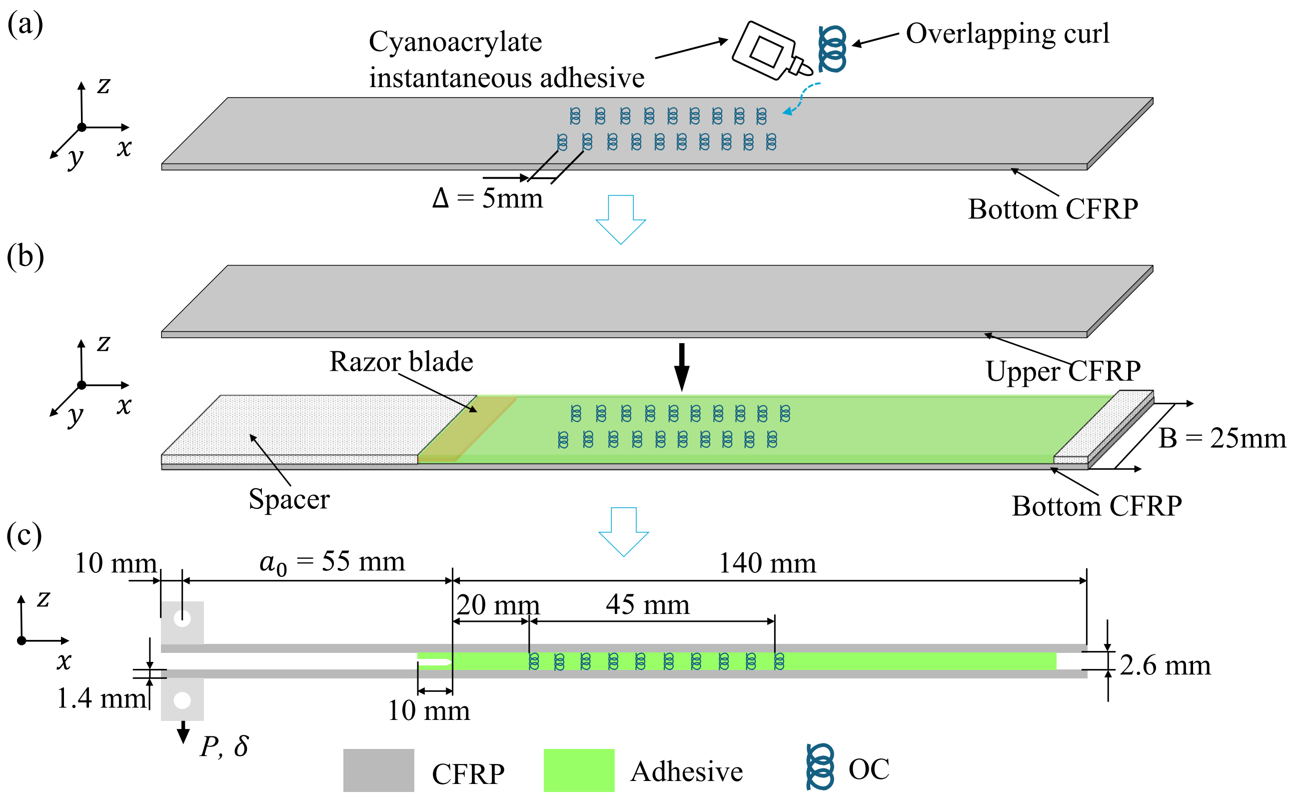

Fig. 2. Schematic illustration of the fabrication process and dimensions of DCB samples with through-thickness OC reinforcements in the adhesive bondline.

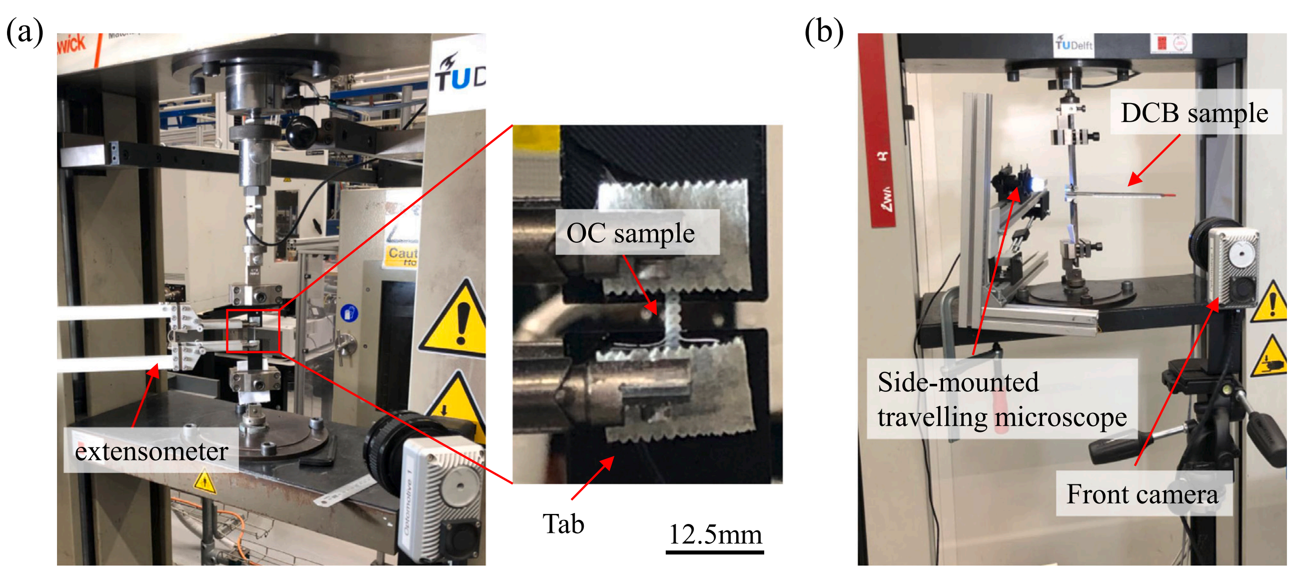

Fig. 3. The experiment setup for (a) overlapping curl tensile test and (b) DCB test.

3.3. Calculation of the energy release rate

The energy release rate (ERR) of the DCB specimen was calculated based on the compliance calibration data reduction method [30]:

$$\text{ERR} = \frac{nP\delta}{2Ba} \cdot \frac{F}{N} \tag{1}$$

where P is the load and δ is the displacement recorded during the DCB testing. B is the specimen width, a is the crack length, n is the exponent of the slope between $log(C/N)$ and $log(a_i)$, where $C = \delta_i/P_i$.

The correction factors of F and N are given as follows:

$$F = 1 - \frac{3}{10}\left(\frac{\delta}{a}\right)^2 - \frac{3}{2}\left(\frac{\delta t}{a^2}\right) \tag{2}$$

$$N = 1 - \left(\frac{L'}{a}\right)^3 - \frac{9}{8}\left[1 - \left(\frac{L'}{a}\right)^2\right]\left(\frac{\delta t}{a^2}\right) - \frac{9}{35}\left(\frac{\delta}{a}\right)^2 \tag{3}$$

where L' is the horizontal distance between center of the loading pin and edge of the loading block ($L' = 5\,\text{mm}$), while t is the vertical distance between the center of the loading pin and the mid-plane of the substrate (t=10 mm). Correction factor F is especially important in specimens when the ratio of opening displacement and crack length

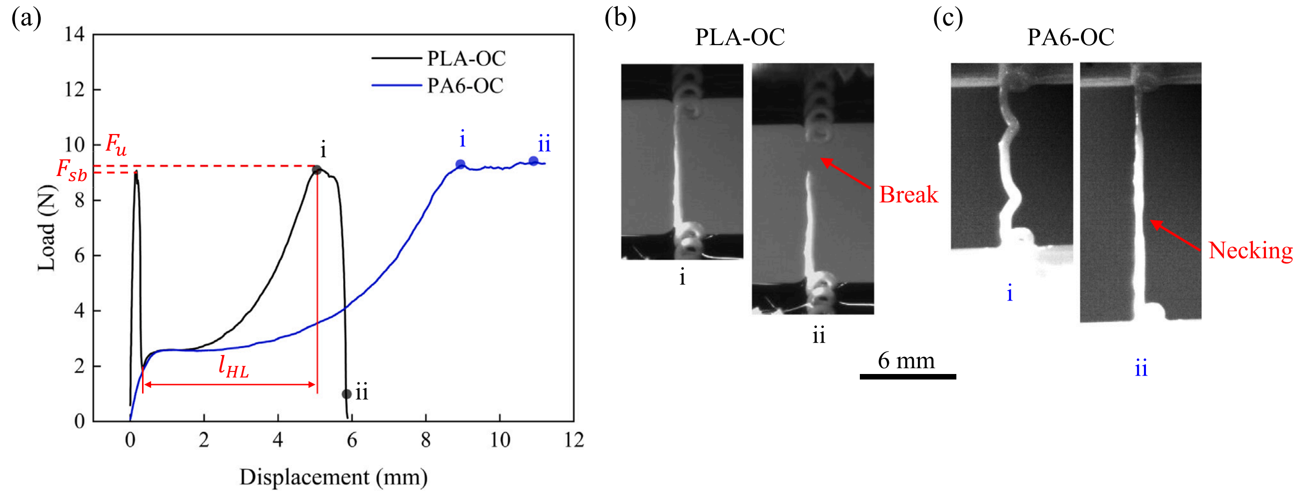

Fig. 4. (a) Representative load–displacement curves of straight fiber and overlapping curl. F_{sb}: the load to break sacrificial bond; F_u: ultimate failure load; l_{HL}: the hidden length due to curl unfolding, defined as the distance between F_{sb} and F_u. The corresponding tensile process snapshots of (b) PLA-OC and (c) PA6-OC at points i and ii.

(δ/a) is above 0.4 [30]. It should be noted that the embedded OCs will generate crack bridging during crack propagation. Therefore, the ERR values calculated using the compliance calibration method represent the apparent fracture resistance of the joint, including contributions from both adhesive fracture and OC-induced crack bridging, rather than the intrinsic fracture toughness of the adhesive layer alone.

4. Results and discussion

4.1. Overlapping curl tensile test results

Fig. 4(a) shows representative load–displacement curves of the 3D-printed overlapping curls. In PLA-OC, a clear sacrificial bond break (F_{sb}) is identified, marked by the first load drop in its load–displacement response. The break of the sacrificial bond is followed by the unfolding of the hidden length l_{HL}. Once the hidden length is completely stretched, the load reaches the maximum failure load F_u at point-i and the OC structure fails (Fig. 4(b)-ii). For the PA6-OC, the behavior is quite distinct. There is no sacrificial bond breakage as the load increases progressively with the displacement. After reaching F_u, the load reaches a plateau region, following the PA6-OC fiber necking (Fig. 4(c)-ii). From these load–displacement curves, it is evident that PLA-OC is more brittle than PA6-OC, as also reported in previous work [26]. It is worth noting that two curls unfolded during tensile testing in this PA6-OC, making it challenging to determine the actual hidden length of one curl. However, the effect of hidden length on the DCB joint energy release rate will be addressed further on.

4.2. DCB test results

Fig. 5 shows the representative experimental load–displacement curves and corresponding ERR-curves of DCB-Pure, DCB-PLA-Straight, and DCB-PA6-Straight. All DCB samples showed cohesive failure. In Fig. 5(a), the three load–displacement curves show similar trends except that the DCB-PLA-Straight has an evident load increase around displacement 50 mm. In the corresponding ERR values of Fig. 5(b), the ERR curves exhibit similar overall trends with crack advance. However, there is an anomalous peak point at crack length 116 mm of DCB-PLA-Straight. The calculated average ERR of these three DCB configurations has no significant difference: $\mathrm{ERR}_{ave}^{\mathrm{Pure}} = 0.72 \pm 0.07\,\mathrm{kJ/m^2}$, $\mathrm{ERR}_{ave}^{\mathrm{PLA\text{-}Straight}} = 0.78 \pm 0.06\,\mathrm{kJ/m^2}$, and $\mathrm{ERR}_{ave}^{\mathrm{PA6\text{-}Straight}} = 0.73 \pm 0.08\,\mathrm{kJ/m^2}$. These results indicate that the integrated PLA-Straight and PA6-Straight fibers do not improve the ERR of the joint.

Fig. 6 shows the representative experimental load–displacement curves and corresponding ERR-curves of DCB-Pure, DCB-PLA-OC, and DCB-PA6-OC. From the load–displacement curves in Fig. 6(a), there are significant differences in the load–displacement curves of the DCB-OC samples in comparison with the DCB-Pure sample. The load-capacities in the DCB-OC joints are higher than DCB-Pure. In addition, DCB-PA6-OC shows higher loads than DCB-PLA-OC at the same displacement. In Fig. 6(b), the ERR values of the OC-integrated DCB samples exhibit sawtooth-like rising and falling patterns. The calculated average ERR of DCB-OC is: $\mathrm{ERR}_{ave}^{\mathrm{PLA\text{-}OC}} = 1.03 \pm 0.14\,\mathrm{kJ/m^2}$ and $\mathrm{ERR}_{ave}^{\mathrm{PA6\text{-}OC}} = 1.30 \pm 0.14\,\mathrm{kJ/m^2}$, which are significantly higher than that of the pure sample ($0.72 \pm 0.07\,\mathrm{kJ/m^2}$). However, as the crack propagates further (crack length $a > 110\,\mathrm{mm}$ of DCB-PLA-OC and $a > 125\,\mathrm{mm}$ of DCB-PA6-OC), the ERR drops and approaches the pure results. When comparing the maximum ERR values reached by the OC reinforcement specimens, we find that the integrated PLA-OC can improve the ERR up to 73 % and PA6-OC can improve up to 119 % compared to the DCB-Pure. Table 2 summarizes the ERR values determined.

4.3. In-situ optical observation

To better understand the influence of integrated straight fiber and overlapping curl on fracture phenomena of the DCB joints, in-situ optical observations from both crack front and crack side views, and corresponding ERR data points are analyzed in Fig. 7 and 8.

In the case of DCB-PLA-Straight shown in Fig. 7(a), the typical behavior is presented in points-1 and 4 where no bridging is triggered after the crack crosses the PLA straight fibers. Hence, no extrinsic toughening mechanisms are triggered and there is no increase in the ERR in comparison with the pure sample. One exception to this typical behavior is shown in the ERR peak point-2. This corresponds to PLA straight fiber bridging that breaks shortly after as the opening displacement increases, leading to an ERR drop in point-3 (the arrows in the in-situ pictures show the bridging and break of the PLA straight fiber). In the case of DCB-PA6-Straight in Fig. 7(b), the PA6 straight fibers are pulled out (e.g., in-situ photos in point-2) of the adhesive layer as the crack propagates and no bridging is triggered. The resulting ERR values are similar to those for the DCB-Pure. Also important to mention that the existence of both the PLA and PA6 straight fibers does not result in a weakening of the crack resistance of the bonded joints when compared to pure adhesive.

Fig. 8 shows the in-situ observations of the DCB-OC samples. For DCB-PLA-OC in Fig. 8(a), as the crack crosses the OC, the sacrificial bonds break and the hidden length unfolds. At point-1, we can

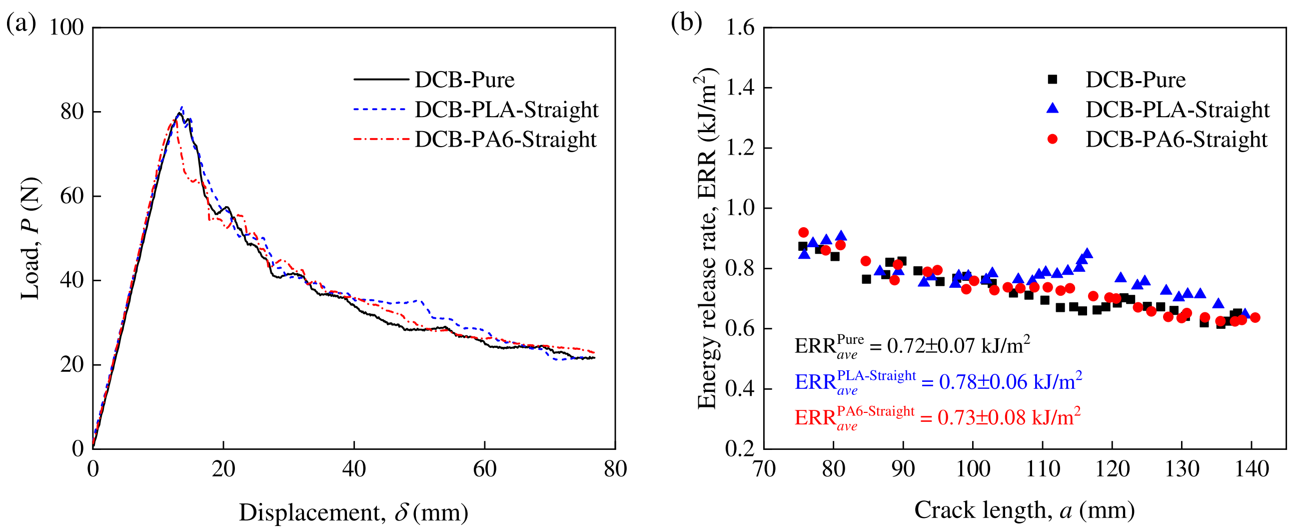

Fig. 5. (a) Representative load–displacement curves of DCB specimens and (b) corresponding energy release rate plots for Pure, integrated PLA-Straight, and integrated PA6-Straight. The straight fiber reinforcement region spans from crack length 75 mm to 120 mm. For the DCB–PLA–Straight and DCB–PA6–Straight specimens, $\delta/a > 0.4$ was reached at displacements of 44.92 mm (a = 112.09 mm) and 51.56 mm (a = 128.06 mm), respectively. The ASTM correction factor was applied for ERR calculations thereafter.

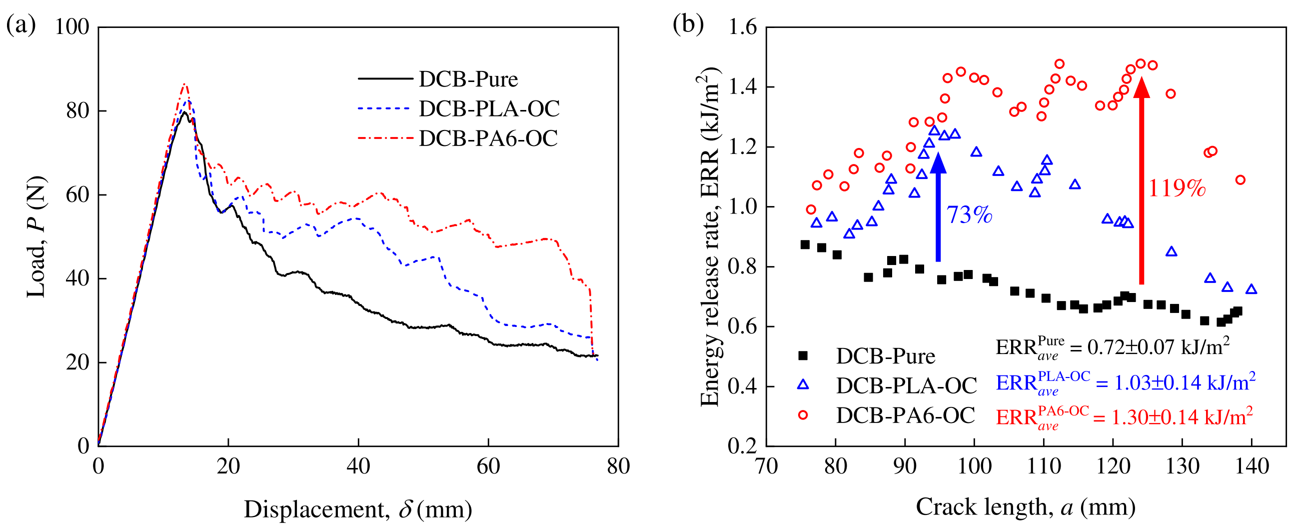

Fig. 6. (a) Representative load–displacement curves of DCB specimens and (b) corresponding energy release rate plots for Pure, integrated PLA-OC, and integrated PA6-OC. The OC reinforcement region spans from crack length 75 mm to 120 mm. For the DCB–PLA–OC and DCB–PA6–OC specimens, $\delta/a > 0.4$ was reached at displacements of 38.22 mm (a = 93.49 mm) and 36.99 mm (a = 91.26 mm), respectively. The ASTM correction factor was applied for ERR calculations thereafter.

Table 2
Summary of obtained ERR values of DCB samples with different reinforcements. ERR_{ave} is the average±standard deviation achieved throughout the ERR-curve. ERR_{max} is the maximum ERR value (due to OC bridging) and ERR_0 is the ERR value of the DCB-Pure sample at the same crack length.

Nomenclature	ERR_{ave} (kJ/m^2)	ERR_{max} (kJ/m^2)	$(ERR_{max} - ERR_0)/ERR_0$
DCB-Pure	0.72 ± 0.07	–	–
DCB-PLA-Straight	0.78 ± 0.06	–	–
DCB-PA6-Straight	0.73 ± 0.08	–	–
DCB-PLA-OC	1.03 ± 0.14	1.25	73 %
DCB-PA6-OC	1.30 ± 0.14	1.48	119 %

observe three PLA OCs bridging simultaneously (as indicated by the solid arrow), which justifies the rising ERR at point-1. As the crack propagates further, two of the OCs break, indicated by the dashed arrows in point-2, and the ERR value drops accordingly. After point-3, the PLA OCs bridging breaks gradually and the ERR decreases. The ERR values return to the pure results at the end in point-4, 20 mm beyond the reinforcement region. In DCB-PA6-OC in Fig. 8(b), at point-1 we can observe eight PA6 OCs bridging simultaneously. The large number of PA6 OC activates a bridging effect that contributes to the high ERR value (1.45 kJ/m^2). Then, some of the PA6 OCs are pulled out from the adhesive layer, followed by the corresponding PA6 OCs bridging breaks in point-2, resulting in a drop in the ERR. As the crack progresses and

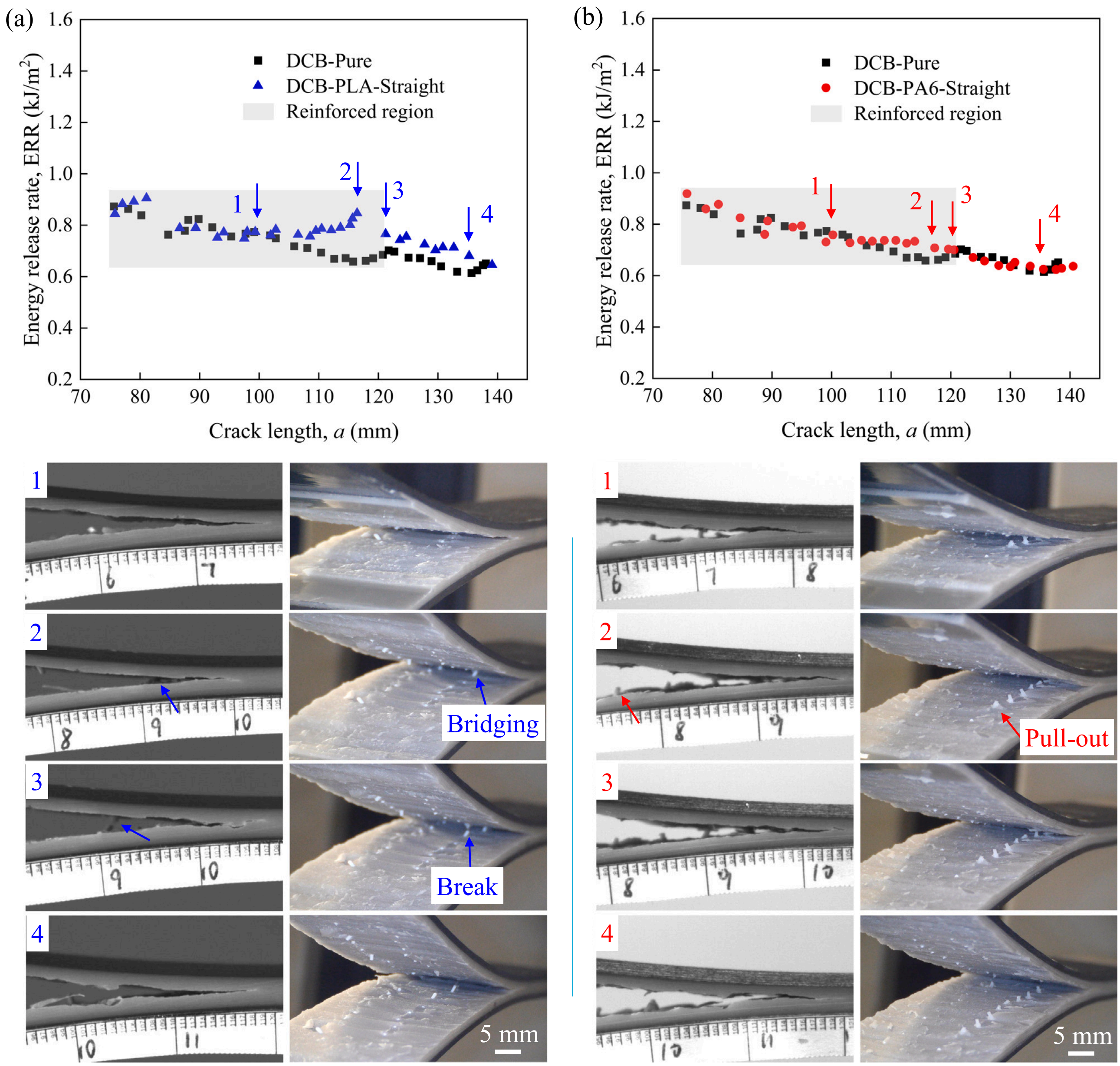

Fig. 7. Typical ERR data points, corresponding in-situ optical observations from the crack front and crack side views of (a) DCB-PLA-Straight and (b) DCB-PA6-Straight. The ERR of DCB-Pure is plotted as a reference. The crack length measured from the pasted grid paper is offset approximately by 25 mm from the actual crack tip position.

crosses the remaining OCs, the ERR increases again, reaching point-3. The same phenomenon is repeated from point-3 to point-4. Owing to the continued unfolding of hidden lengths of PA6 OCs, a broad bridging zone is sustained prior to point-4, leading to a steady rise in ERR. After point-4, as the existing OC bridging gradually diminishes and no new bridging is activated, the ERR of the DCB-PA6-OC converges towards the DCB-Pure.

From the above in-situ observations, we conclude that the topology of OC is crucial for activating the bridging effect, whereas the straight fiber topology provides no toughening. Moreover, the F_{sb} in the PLA OC does not significantly affect the ERR in the experiment. The saw-tooth patterns in the DCB-OC ERR results are caused by the activation and failure of bridging OCs during the crack propagation. More PA6 OC bridging is activated at the same time than that of PLA OC and PA6 OC shows higher ERR improvement.

4.4. Anchoring of the adhesive layer and reinforcements

In order to elucidate the effects of reinforcement material and topology on bridging activation and the corresponding variations in ERR enhancement, Fig. 9 shows representative in-situ observations and fracture surface of the DCB samples, highlighting the primary failure modes associated with integrated straight fibers and overlapping curls. The scanning electron micrograph (SEM) images in the rightmost column of Fig. 9 illustrate the structural differences of the straight fibers and overlapping curls. Furthermore, Fig. 10 presents SEM images of the fracture morphologies of integrated PLA and PA6 straight fibers and overlapping curls in the DCB samples after testing, revealing the distinctive interactions between the reinforcements and the adhesive matrix.

For the DCB-PLA-Straight sample in Fig. 9(a), two typical failure modes are observed: fiber pull-out and fiber break. The cylindrical

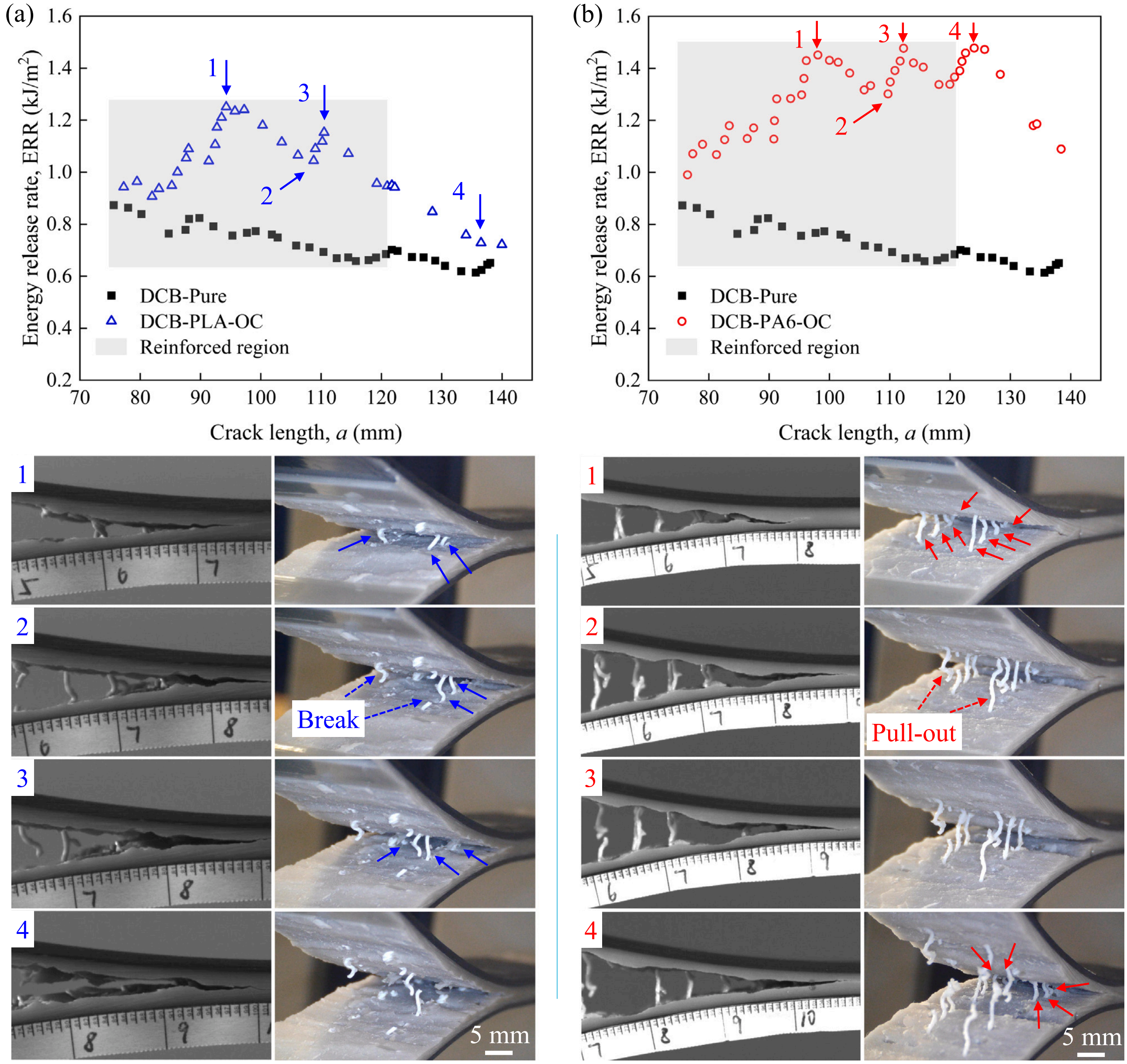

Fig. 8. Typical ERR data points, corresponding in-situ optical observations from the front and side views of (a) DCB-PLA-OC and (b) DCB-PA6-OC. The ERR of DCB-Pure is plotted as a reference. The solid arrows in the in-situ pictures indicate the bridging overlapping curls. The dashed arrows in the in-situ pictures indicate the broken bridging overlapping curls.

geometry of the straight fiber contributes to its easy pull-out failure, although a few PLA fibers adhere to the adhesive and ultimately fracture, leading to limited bridging effects (see point-2 in Fig. 7(a)). On the other hand, all fibers in the DCB-PA6-Straight (Fig. 9(b)) show pull-out failure mode, consistent with the poor interfacial adhesion of PA6 with epoxies [31], which prevents any bridging effect. The contrasting failure modes of PLA and PA6 straight fibers are therefore attributed to differences in interfacial adhesion with the adhesive matrix. SEM images of the fracture morphologies (Fig. 10(a–c)) further support this interpretation: PLA straight fibers exhibit rough surfaces in both pulled-out and fractured states, whereas PA6 straight fibers display smooth surfaces, confirming stronger PLA–adhesive interfacial adhesion.

In the case of DCB-PLA-OC, shown in Fig. 9(c), three failure modes can be identified: (i) OC fracture after hidden-length unfolding, (ii) premature OC fracture before hidden-length unfolding, and (iii) OC interfacial failure. These observations highlight the critical role of the OC topology, which not only provides hidden length for crack bridging but also anchors the reinforcement within the adhesive layer. The OC structure contains three curls, with the top and bottom curls filled with adhesive (Fig. 10(d)), forming mechanical interlocks that secure the OC within the bondline. As the crack propagates, the central curl is firstly exposed to the crack tip following sacrificial bond break and hidden length unfolding, subsequently contributing to crack bridging-failure mode (i). In terms of material effect, the fact that PLA fiber is more brittle than PA6 fiber makes it more prone to premature failure before unfolding of the hidden length [26], limiting the extended bridging effect. In addition, the stronger PLA–adhesive interfacial adhesion promotes efficient stress transfer from the adhesive layer to the OC. While enhanced stress transfer is generally beneficial, it also increases the likelihood of premature fracture in a relatively brittle reinforcement, leading to failure mode (ii), as shown in Fig. 10(e). Occasional interfacial failure (failure mode (iii)) was also observed when a defect occurs in the interfaces between the PLA-OC and the CFRP substrate. In contrast, the superior ductility of PA6, combined

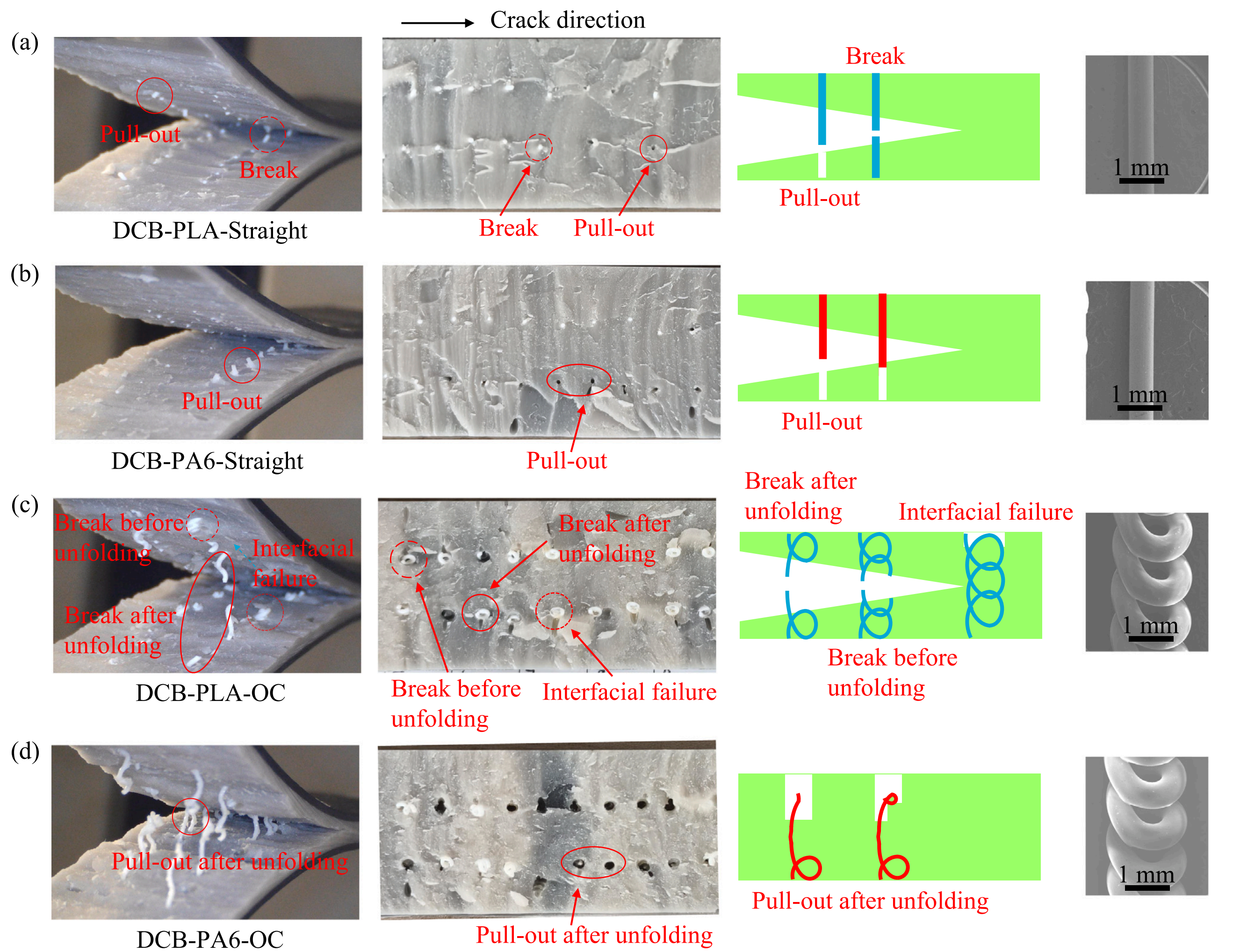

Fig. 9. Representative failure modes of the integrated straight fiber and overlapping curl structure from in-situ observations, fracture surfaces, and corresponding schematics. The scanning electron micrograph of straight fiber and overlapping curl structures is in the rightmost column.

with its relatively weak adhesion to the epoxy adhesive, favors extensive hidden length unfolding and stable crack bridging. The typical failure mode of DCB-PA6-OC specimens is OC pull-out after substantial hidden length unfolding. From Fig. 9(d), we observe clear voids from the fracture surface, indicating that the PA6 overlapping curl pulls out and does not undergo early breakage. The hidden length within the central curl is therefore able to fully unfold before eventual detachment of one OC end from the adhesive layer (Fig. 10(f)). Although the lower PA6–adhesive adhesion may reduce load-transfer efficiency, it also decreases the tendency for premature fiber fracture. Together with the high ductility of PA6, this enables longer crack bridging distances and more complete activation of the SBHL mechanism. Consequently, the overall toughening performance is governed by a balance between load-transfer efficiency and hidden length activation, with the latter playing the dominant role in the present OC design. This explains why the PA6 OCs achieve a greater ERR enhancement than their PLA counterparts.

An important observation from the DCB–PA6–OC experimental bridging filament image (Fig. 9(d)) is that, after pull-out, the PA6 OCs remain attached to both the upper and lower CFRP substrates. As described in Section 2.3, during the fabrication of the DCB–OC specimens, the OCs were initially bonded only to the bottom CFRP substrate using a cyanoacrylate instantaneous adhesive. This adhesive was applied in a very thin layer and served solely to align and position the OCs on the substrate. This observation further indicates that the actual anchoring of the overlapping curls is primarily governed by the mechanical interaction between the curl geometry and the adhesive layer, consistent with the schematic illustration.

5. Numerical modeling

In the above experimental DCB results, the overlapping curl bridging effect was successfully triggered and a significant improvement in the energy release rate in comparison with the DCB-Pure sample was achieved. In this section, a finite element model is built to explore further the OC bridging effects beyond experimental manufacturing limitations and to expand the design space to investigate the failure load F_u and hidden length l_{HL} effects on the joint energy release rate improvement. It should be noted that the present parametric study focuses exclusively on the effects of failure load and hidden length. Other factors, such as OC density, spacing, interfacial adhesion, topology, and reinforcement region length, may also influence the fracture response and warrant further investigation in future work.

5.1. DCB finite element model

A 3D model was built in ABAQUS 2021 to simulate the DCB test shown in Fig. 11(a). The CFRP substrate with 1.4 mm thickness is assumed orthotropic and linear elastic, with E_{xx} = 141 000 MPa, E_{yy} = E_{zz} = 9750 MPa, ν_{xy} = ν_{xz} = 0.267, ν_{yz} = 0.5, G_{xy} = G_{xz} = 5200 MPa, and G_{yz} = 3190 MPa [29]. The adhesive layer thickness is 2.6 mm with elastic–plastic property of the used Araldite 2015/1 adhesive (young's

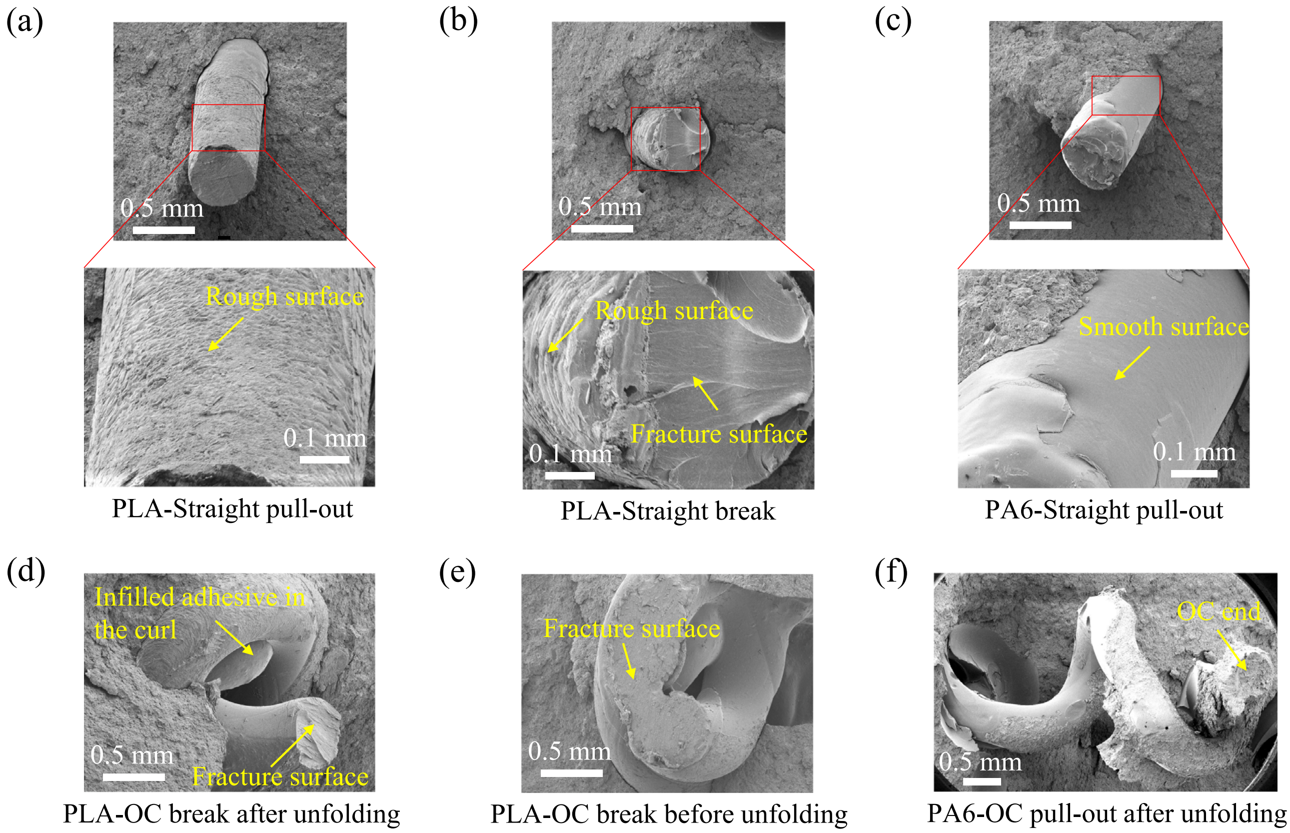

Fig. 10. Fracture morphologies under SEM for representative failure modes of the integrated straight fiber and overlapping curl structure.

modulus: 1790 MPa, yield strength: 16.17 MPa, and fracture strength: 30.86 MPa) taken from [32]. Both the CFRP substrate and adhesive were modeled with eight-node brick elements (C3D8). The cohesive failure within the fracture surface was simulated using the eight-node three-dimensional cohesive elements (COH3D8) with a finite thickness 0.01 mm located at the center of the adhesive layer. A bi-linear traction separation law was implemented into the model to predict crack growth and degradation based on the MAXStress crack criterion. The energy release rate was the average value 0.72 kJ/m^2 of the DCB-Pure experiment. The stiffness of the cohesive elements was set to 1×10^5 N/mm and the maximum traction was defined as 30.86 MPa, corresponding to the adhesive fracture strength. The boundary conditions were applied to the reference points: RP1 and RP2, coupling with the left edges of the DCB substrates. The degrees of freedom in the DCB ends were fixed. A mesh sensitivity was conducted and mesh size was chosen as $0.4 \times 0.4 \times 0.4$ around the crack path and $0.8 \times 0.8 \times 0.4$ in the other region.

5.2. Numerical parametric study

5.2.1. Model verification

Fig. 12(a) compares the load–displacement curves of the DCB-Pure from experiment and numerical simulation. In the initial region, the experimental load is higher than the simulated one, whereas in the final region it is lower. This difference arises because the experimental ERR curve shows a slight decrease, while the simulation uses the average ERR as input. Consequently, the simulated ERR is underestimated in the initial region and overestimated in the final region, leading to the observed load evolution discrepancy. Overall, the numerical model reproduces the DCB load–displacement response well, accurately capturing the cohesive failure behavior.

The OCs were added to the model in the same positions as in the DCB experimental samples: 2 along the width and 10 along the length with 5 mm spacing as shown in Fig. 11. In total, 20 (10×2) overlapping curls were added to the model. The reinforcement region is located from the crack length 75 mm to 120 mm. To simplify the overlapping curl simulation input, we linearize the load–displacement of OC response from zero to the failure load F_u followed by a load drop to zero, as shown in Fig. 12(b). The load drop at a displacement of $d_p = 0.35$ mm is introduced to prevent convergence issues in the simulation caused by the abrupt load decrease due to OC failure. The overlapping curl response was simulated by the spring element which has also been applied to reproduce the similar behavior of Z-pins in composite laminates [33]. As part of a parametric study on the effect of overlapping curl mechanical properties on the DCB response, two key parameters, failure load F_u and hidden length l_{HL}, are analyzed. Specifically, F_u was set to 1, 4, 8, and 16 N, while l_{HL} was varied at 3, 6, 9, and 12 mm, as summarized in the Table 3. These values were selected based on the experimentally measured OC properties (F_u = 9.26 N and l_{HL} = 8.96 mm) shown in Fig. 12(b). It should be noted that the spring representation does not explicitly capture sacrificial bond failure or progressive deformation of the OC. Instead, it is intended to isolate the effects of the two key crack bridging parameters: failure load and hidden length. Since hidden length unfolding followed by pull-out was the dominant toughening mechanism observed for the PA6 OCs, the simplified spring model was considered sufficient to capture the primary contribution of the reinforcement to ERR enhancement. For the overlapping curl sacrificial bond load-capacity F_{sb} effect on the numerically simulated results, the readers can refer to the supplementary data.

5.2.2. Typical overlapping curl bridging mechanisms

The typical load–displacement, ERR response (F_u = 8, 16 N and l_{HL} = 3, 6 mm), and crack propagation schematic of DCB-F_u8N-l_{HL}3 mm simulations are illustrated in Fig. 13. The DCB-Pure simulation result is plotted for reference. In Fig. 13, compared to DCB-Pure, these DCB-OC

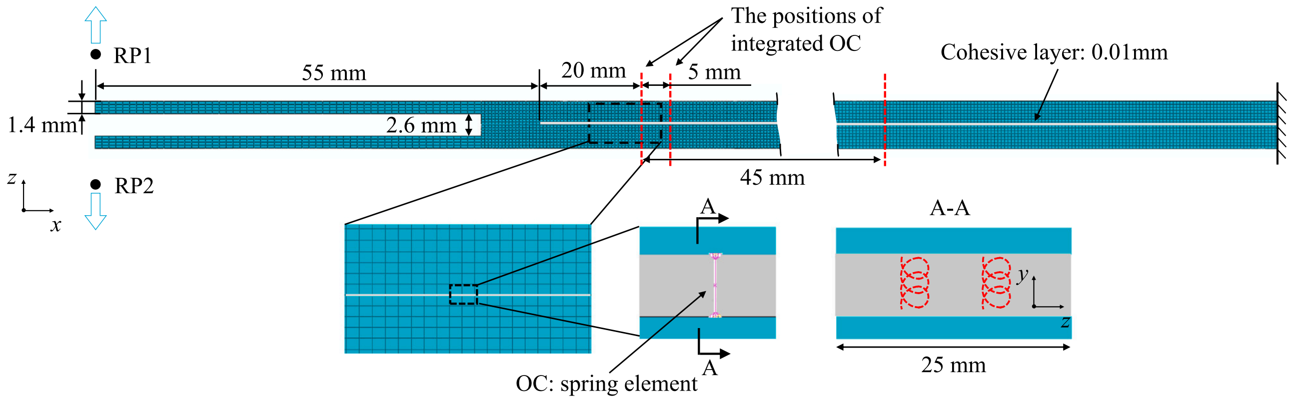

Fig. 11. The geometry, boundary condition, and mesh of the DCB numerical model.

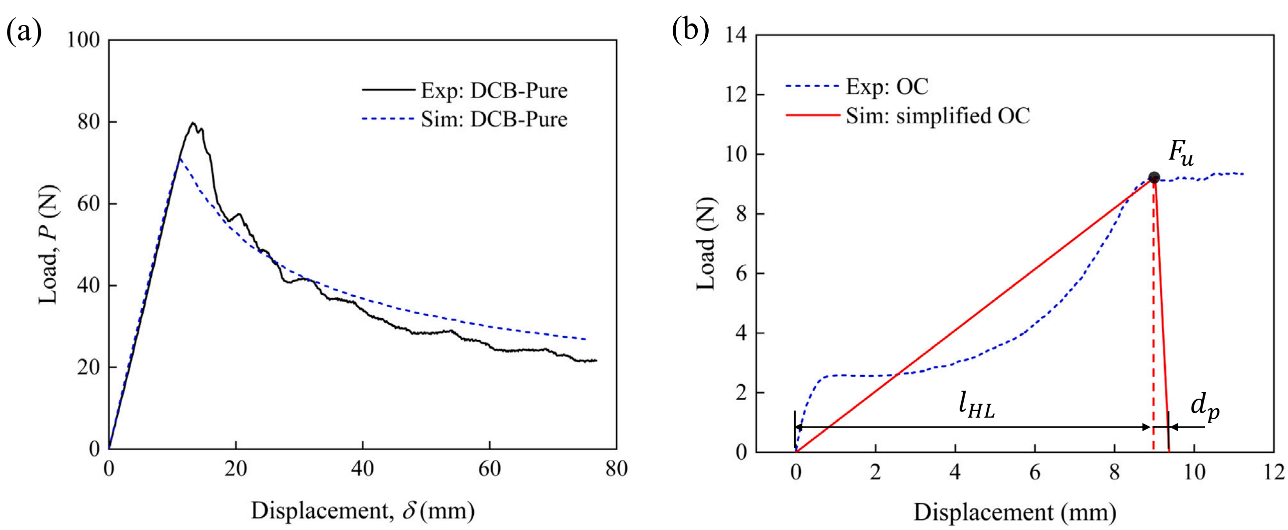

Fig. 12. (a) Model validation by comparing the experimental vs numerical DCB-Pure load–displacement curves. (b) The simplified overlapping curl experimental load–displacement response as input for simulations.

Table 3
Overlapping curl parameters for the numerical parametric study.

Simulated parameters	Values
Overlapping curl failure load, F_u (N)	1, 4, 8, 16
Overlapping curl hidden length, l_{HL} (mm)	3, 6, 9, 12

joints start to show a load increase around a displacement of 22 mm due to OC bridging. The subsequent fluctuations in load-capacity are caused by the failure of bridging OCs and the activation of new ones as the crack propagates, in a similar behavior as observed in the experiments in Fig. 6. When the overlapping curl failure load F_u is fixed at 8 N, a longer overlapping curl hidden length (l_{HL} = 6 mm) results in a slower load increase (within displacement 22 mm–35 mm) compared to the shorter hidden length (l_{HL} = 3 mm), owing to the reduced OC stiffness (i.e., smaller F_u–l_{HL} slope). However, the OC with longer l_{HL} can bridge over a greater distance as the crack propagates, activating more OCs and leading to a higher load-capacity in the joint after 38 mm. Conversely, when l_{HL} = 3 mm is fixed, a higher failure load (e.g., F_u = 16 N) in DCB-F_u16N-l_{HL}3 mm allows the joint to sustain higher load-capacity than DCB-F_u8N-l_{HL}3 mm. Once all OCs fail (around 70 mm displacement), the load response returns to the level of the DCB-Pure joint.

Regarding the ERR-curves in Fig. 13(b), when the crack tip reaches the OC-reinforced region at the crack length of 75 mm and the OC starts to bridge the crack, the ERR increases accordingly. Similar to the load response, the ERR continues to fluctuate following its maximum value, ERR_{max}, at point-1, exhibiting trends consistent with the load–displacement curves. Taking the deformation process of DCB-F_u8N-l_{HL}3 mm as an example, 8 OCs (4 × 2 OCs) are simultaneously engaged in load transfer and crack bridging at this stage, as illustrated in Fig. 13(c). After all the integrated OCs fail from point-2 onward, the ERR drops back to point-3 as in the DCB-Pure results.

5.2.3. F_u and l_{HL} effects

The results of the parametric study are presented in Fig. 14(a) and (b), showing the maximum energy release rate (ERR_{max}) obtained for each design combination and the corresponding crack propagation distance within the reinforced region (a-a_{OC}) required to reach this maximum value, respectively. The former is critical for understanding the maximum potential of the OC toughening mechanisms, while the latter provides insight into the crack propagation length required to fully develop this potential.

From Fig. 14(a), ERR_{max} increases both with the failure load F_u and hidden length l_{HL}. When the failure load is low (e.g., F_u = 1 N), even with an increase in hidden length, ERR_{max} shows limited improvement compared to ERR_{Pure}. As the F_u increases further, the ERR_{max} improvement becomes more pronounced. Especially, at the highest values of F_u = 16 N and l_{HL} = 12 mm, ERR_{max} reaches to 2 kJ/m^2, which is 2.77 times higher than ERR_{Pure}. This demonstrates that a significant improvement in ERR can be achieved when the OC has a great failure load and a long hidden length. Looking into Fig. 14(b) on the crack propagation

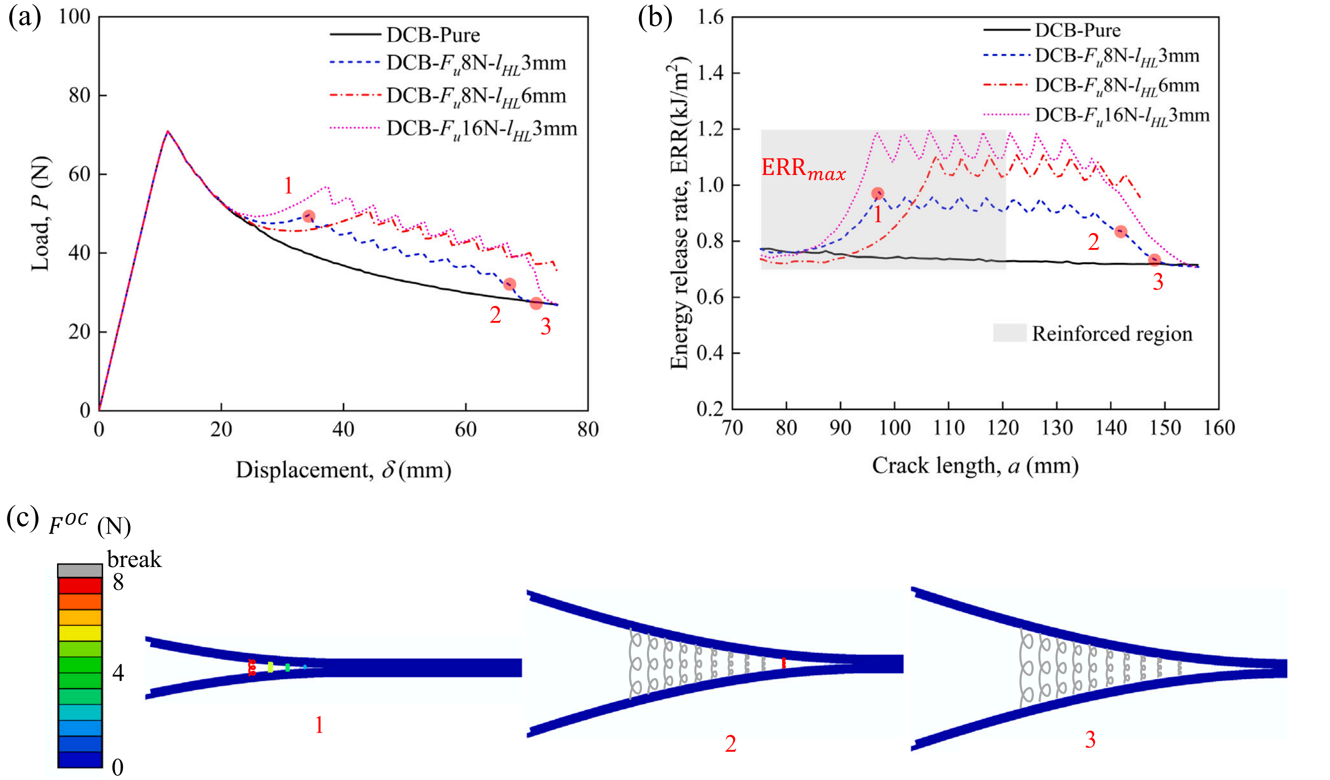

Fig. 13. (a) The simulated load–displacement and (b) ERR curve of DCB-OC joints with F_u =8, 16 N and l_{HL} = 3, 6 mm. The DCB-Pure is plotted as a reference. (c) The typical points marked in (a) and (b) show the bridging OCs in the joint (only a portion of the DCB arms is shown due to figure size). F^{OC} is the bridging load in each bridging OC.

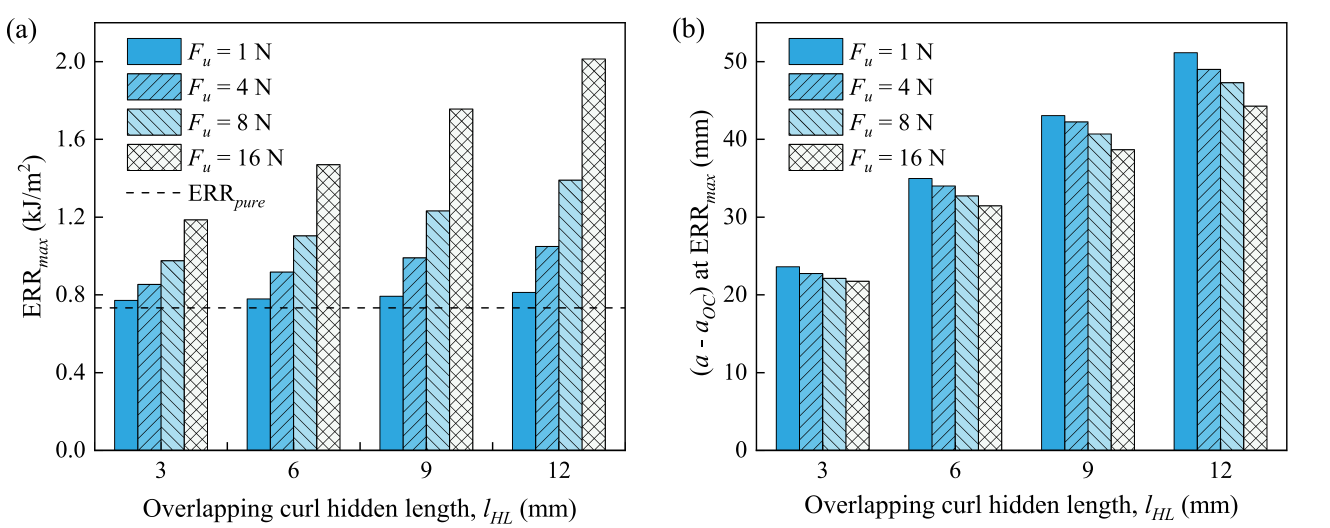

Fig. 14. Effects of F_u and l_{HL} on (a) ERR$_{max}$ in DCB–OC joints and (b) the crack propagation distance within the OC-reinforced region at ERR$_{max}$. a_{OC} denotes the crack length at which the crack tip first enters the OC-reinforced region.

distance a-a_{OC}, it exhibits a different trend. When l_{HL} increases, the corresponding value of a-a_{OC} also increases, indicating that a longer hidden length requires a larger crack propagation distance to reach ERR$_{max}$. On the other hand, for a fixed l_{HL}, increasing F_u reduces the value of a-a_{OC}, thereby restricting crack propagation. This observation provides useful guidance for the design of OC-reinforced joints in engineering applications. If the joint allows sufficient crack propagation distance, enhancing either the OC failure load or the hidden length can effectively improve its fracture resistance. However, in most engineering applications, the allowable crack propagation distance is limited. Therefore, increasing the maximum ERR value of the OC toughening mechanisms comes with a cost: a large crack length. Careful design should be performed on the OC structures in order to balance the maximum ERR achieved and the maximum crack length allowed in the structures.

6. Conclusions

In this work, we explore a novel adhesive bondline architecture by integrating spider silk-inspired, through-thickness overlapping curl structures into the adhesive layer to enhance the fracture resistance of composite joints. The OCs, 3D-printed from two materials (PLA and PA6), are aligned through the adhesive bondline thickness and oriented perpendicular to the crack propagation direction, enabling effective activation of the sacrificial bonds and hidden lengths toughening mechanism under mode I opening loading. The OC topology is critical to this toughening effect, as it anchors the OCs within the adhesive layer and suppresses premature pull-out, in contrast to straight fiber reinforcements. As a result, the unfolding of hidden lengths promotes stable and extended crack bridging distances, allowing multiple OCs to act simultaneously. This synergistic bridging response effectively retards crack propagation and leads to a significant enhancement of the energy release rate. Owing to the PA6 material's superior ductility and resistance to premature failure, PA6 OC contributes to a greater enhancement in fracture resistance than PLA OC. The maximum ERR of the joint increased by up to 119 % with PA6 OC, compared to 73 % with PLA OC. An expansion of the design space using numerical simulations shows that increasing either the failure load or the hidden length of the OC can improve the maximum ERR of the joint. However, achieving a higher maximum ERR requires longer crack propagation when the hidden length is excessively large. Therefore, the OC reinforcement must be carefully designed, especially for joints with limited crack growth allowance.

This study, for the first time, demonstrates composite bonded joints reinforced with 3D-printed through-thickness overlapping curl structures, establishing a robust extrinsic toughening strategy for adhesively bonded composites. Importantly, this approach preserves the mechanical integrity of the CFRP substrates and offers a promising design pathway towards damage-tolerant composite engineering structures. Future lines of work could focus on optimization of OC geometries, use of high strength reinforcement materials, and the performance of the proposed architecture under mixed-mode, fatigue, and environmental loading conditions.

CRediT authorship contribution statement

Zhiyuan Xu: Writing – original draft, Methodology, Data curation, Conceptualization. **Ran Tao:** Writing – review & editing, Visualization, Validation, Methodology, Conceptualization. **Kunal Masania:** Writing – review & editing, Visualization, Validation, Supervision, Methodology, Conceptualization. **Sofia Teixeira de Freitas:** Writing – review & editing, Visualization, Validation, Supervision, Methodology, Conceptualization.

Declaration of competing interest

The authors declare that they have no known competing financial interests or personal relationships that could have appeared to influence the work reported in this paper.

Acknowledgments

The authors gratefully acknowledge the financial support from the China Scholarship Council (No. CSC202107720061). The authors acknowledge Fundacao para a Ciencia e a Tecnologia (FCT) for its financial support via LAETA (project https://doi.org/10.54499/UID/50022/2025).

Appendix A. Supplementary data

Supplementary material related to this article can be found online at https://doi.org/10.1016/j.tafmec.2026.105843.

Data availability

The Data is available on the DOI: 10.4121/35b19ead-8133-4255-99e9-adc14222b738.

References

[1] B. Ravichandran, M. Balasubramanian, Joining methods for fiber reinforced polymer (FRP) composites- a critical review, Compos. Part A: Appl. Sci. Manuf. (2024) 108394.

[2] K.B. Katnam, L. Da Silva, T. Young, Bonded repair of composite aircraft structures: A review of scientific challenges and opportunities, Prog. Aerosp. Sci. 61 (2013) 26–42.

[3] A. Yudhanto, M. Almulhim, F. Kamal, R. Tao, L. Fatta, M. Alfano, G. Lubineau, Enhancement of fracture toughness in secondary bonded CFRP using hybrid thermoplastic/thermoset bondline architecture, Compos. Sci. Technol. 199 (2020) 108346.

[4] J. Kupski, S.T. De Freitas, Design of adhesively bonded lap joints with laminated CFRP adherends: Review, challenges and new opportunities for aerospace structures, Compos. Struct. 268 (2021) 113923.

[5] T. Löbel, D. Holzhüter, M. Sinapius, C. Hühne, A hybrid bondline concept for bonded composite joints, Int. J. Adhes. Adhes. 68 (2016) 229–238.

[6] A. Li, Y. Lyu, B. Yang, D. Yang, Novel repair of bolted composite joints using 3D printed continuous fibre patches with custom fibre paths, Compos. Part B: Eng. (2025) 112212.

[7] Y. Chu, L. Sun, B. Zhan, X. Yang, C. Zhang, W. Huang, Static and dynamic behavior of unbalanced bonded joints with adhesion defects in automotive structures, Compos. Struct. 226 (2019) 111234.

[8] S. Teixeira de Freitas, D. Zarouchas, J. Poulis, The use of acoustic emission and composite peel tests to detect weak adhesion in composite structures, J. Adhes. 94 (9) (2018) 743–766.

[9] M. Kadlec, R. Růžek, P. Bělský, Concurrent use of Z-pins for crack arrest and structural health monitoring in adhesive-bonded composite lap joints, Compos. Sci. Technol. 188 (2020) 107967.

[10] A. Yudhanto, G. Lubineau, I.A. Ventura, N. Watanabe, Y. Iwahori, H. Hoshi, Damage characteristics in 3D stitched composites with various stitch parameters under in-plane tension, Compos. Part A: Appl. Sci. Manuf. 71 (2015) 17–31.

[11] A. Mouritz, Review of z-pinned composite laminates, Compos. Part A: Appl. Sci. Manuf. 38 (12) (2007) 2383–2397.

[12] K. Maloney, N. Fleck, Toughening strategies in adhesive joints, Int. J. Solids Struct. 158 (2019) 66–75.

[13] S. Heide-Jørgensen, S.T. de Freitas, M.K. Budzik, On the fracture behaviour of CFRP bonded joints under mode I loading: Effect of supporting carrier and interface contamination, Compos. Sci. Technol. 160 (2018) 97–110.

[14] R. Tao, X. Li, A. Yudhanto, M. Alfano, G. Lubineau, Toughening adhesive joints through crack path engineering using integrated polyamide wires, Compos. Part A: Appl. Sci. Manuf. 158 (2022) 106954.

[15] F. Delzendehrooy, M. Ayatollahi, A. Akhavan-Safar, L. Da Silva, Strength improvement of adhesively bonded single lap joints with date palm fibers: Effect of type, size, treatment method and density of fibers, Compos. Part B: Eng. 188 (2020) 107874.

[16] H. Wan, N. Leung, S. Algharaibeh, T. Sui, Q. Liu, H.-X. Peng, B. Su, Cost-effective fabrication of bio-inspired nacre-like composite materials with high strength and toughness, Compos. Part B: Eng. 202 (2020) 108414.

[17] Z. Yin, F. Hannard, F. Barthelat, Impact-resistant nacre-like transparent materials, Science 364 (6447) (2019) 1260–1263.

[18] X. Zhang, J. Wang, L. He, Y. Ni, Bioinspired hybrid design of transparent architectured glass for improved comprehensive impact performance, Compos. Part B: Eng. (2025) 112245.

[19] A. Wagih, R. Tao, G. Lubineau, Bio-inspired adhesive joint with improved interlaminar fracture toughness, Compos. Part A: Appl. Sci. Manuf. 149 (2021) 106530.

[20] I. Kaiser, C. Tan, K. Tan, Bio-inspired patterned adhesive single-lap joints for CFRP and titanium, Compos. Part B: Eng. 224 (2021) 109182.

[21] B. Schmuck, G. Greco, T.B. Pessatti, S. Sonavane, V. Langwallner, T. Arndt, A. Rising, Strategies for making high-performance artificial spider silk fibers, Adv. Funct. Mater. 34 (35) (2024) 2305040.

[22] S. Zou, D. Therriault, F.P. Gosselin, Toughening elastomers via microstructured thermoplastic fibers with sacrificial bonds and hidden lengths, Extrem. Mech. Lett. 43 (2021) 101208.

[23] S. Zou, D. Therriault, F.P. Gosselin, Spiderweb-inspired, transparent, impact-absorbing composite, Cell Rep. Phys. Sci. 1 (11) (2020).

[24] Z. Xu, R. Tao, K. Masania, S.T. de Freitas, Bio-inspired overlapping curl structures for toughening bio-based epoxy: A study on the fracture phenomena, Compos. Sci. Technol. (2025) 111374.

[25] R. Tao, Z. Xu, S. Teixeira de Freitas, Mode I toughening of bio-based epoxy adhesive through 3D-printed biomimetic reinforcements, Compos. PartB: Eng. (2026) 113313.

[26] Z. Xu, R. Tao, K. Masania, S.T. de Freitas, Biomimetic toughening design of 3D-printed polymeric structures: Enhancing toughness through sacrificial bonds and hidden lengths, Mater. Des. 247 (2024) 113361.

[27] N.M. Ribe, M. Habibi, D. Bonn, Liquid rope coiling, Annu. Rev. Fluid Mech. 44 (1) (2012) 249–266.

[28] S. Teixeira de Freitas, D. Zarouchas, J. Poulis, The use of acoustic emission and composite peel tests to detect weak adhesion in composite structures, J. Adhes. 94 (9) (2018) 743–766.

[29] R. Lima, R. Tao, A. Bernasconi, M. Carboni, N. Carrere, S.T. De Freitas, Uncovering the toughening mechanisms of bonded joints through tailored CFRP layup, Compos. Part B: Eng. 263 (2023) 110853.
[30] ASTM D5528. Standard test method for mode I interlaminar fracture toughness of unidirectional fiber-reinforced polymer matrix composites, 2013.
[31] D. Pappas, A. Bujanda, J.D. Demaree, J.K. Hirvonen, W. Kosik, R. Jensen, S. McKnight, Surface modification of polyamide fibers and films using atmospheric plasmas, Surf. Coat. Technol. 201 (7) (2006) 4384–4388.
[32] R.L. Fernandes, S.T. de Freitas, M.K. Budzik, J.A. Poulis, R. Benedictus, From thin to extra-thick adhesive layer thicknesses: Fracture of bonded joints under mode I loading conditions, Eng. Fract. Mech. 218 (2019) 106607.
[33] Y. Gong, X. Chen, L. Zou, X. Li, L. Zhao, J. Zhang, N. Hu, Experimental and numerical investigations on the mode I delamination growth behavior of laminated composites with different z-pin fiber reinforcements, Compos. Struct. 287 (2022) 115370.